ACS Photonics

DECEMBER 2021
VOLUME 8
NUMBER 12
pubs.acs.org/photonics

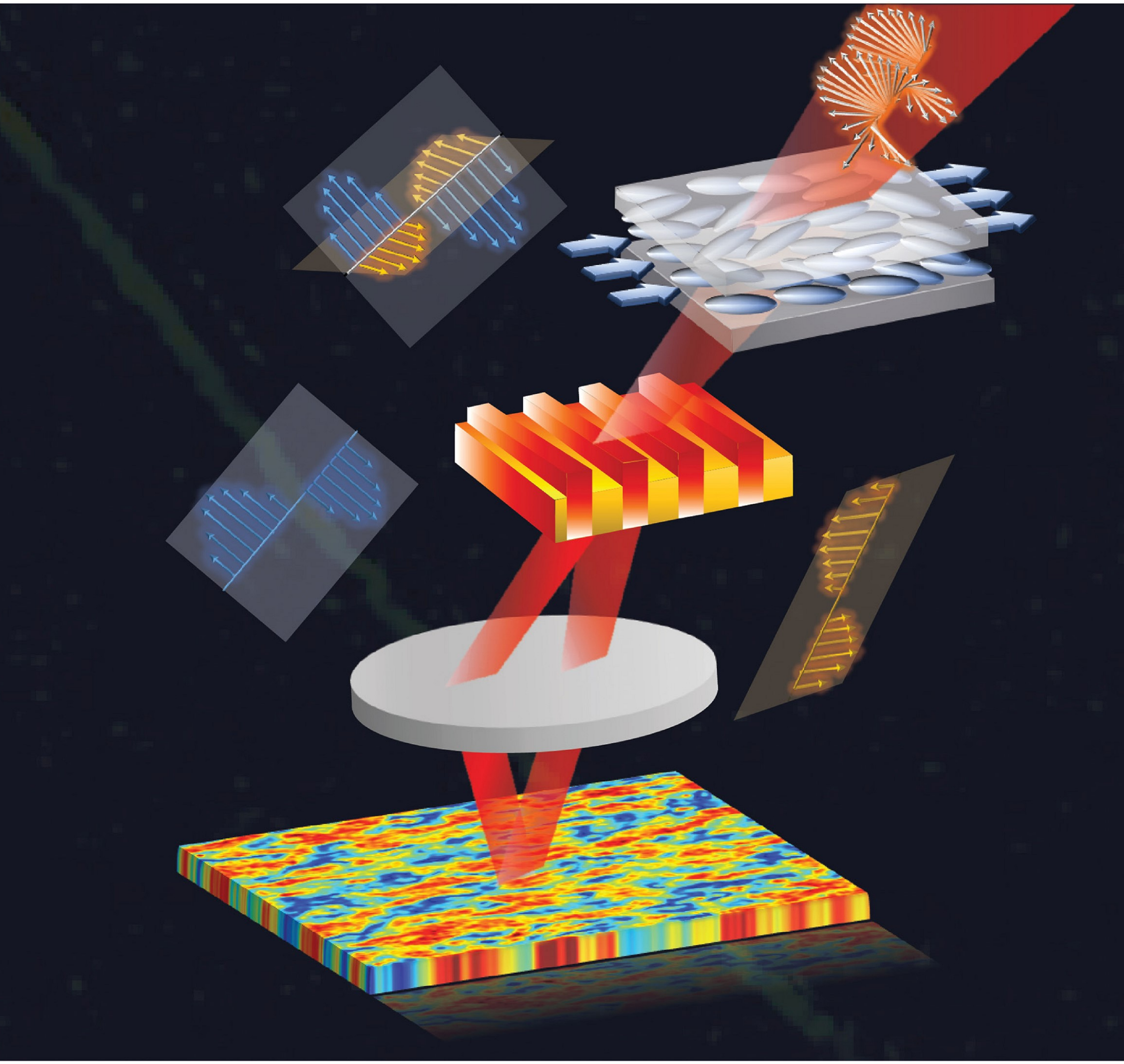

ACS Photonics

pubs.acs.org/journal/apchd5

Letter

Single-Shot Quantitative Polarization Imaging of Complex Birefringent Structure Dynamics

Baoliang Ge,[#] Qing Zhang,[#] Rui Zhang, Jing-Tang Lin, Po-Hang Tseng, Che-Wei Chang, Chen-Yuan Dong, Renjie Zhou, Zahid Yaqoob, Irmgard Bischofberger, and Peter T. C. So*

Cite This: *ACS Photonics* 2021, 8, 3440–3447

Read Online

ACCESS | Metrics & More | Article Recommendations | Supporting Information

ABSTRACT: Polarization light microscopes are powerful tools for probing molecular order and orientation in birefringent materials. While a number of polarization microscopy techniques are available to access steady-state properties of birefringent samples, quantitative measurements of the molecular orientation dynamics on the millisecond time scale have remained a challenge. We propose polarized shearing interference microscopy (PSIM), a single-shot quantitative polarization imaging method, for extracting the retardance and orientation angle of the laser beam transmitting through optically anisotropic specimens with complex structures. The measurement accuracy and imaging performance of PSIM are validated by imaging a birefringent resolution target and a bovine tendon specimen. We demonstrate that PSIM can quantify the dynamics of a flowing lyotropic chromonic liquid crystal in a microfluidic channel at an imaging speed of 506 frames per second (only limited by the camera frame rate), with a field-of-view of up to 350 × 350 μm^2 and a diffraction-limit spatial resolution of ~2 μm. We envision that PSIM will find a broad range of applications in quantitative material characterization under dynamical conditions.

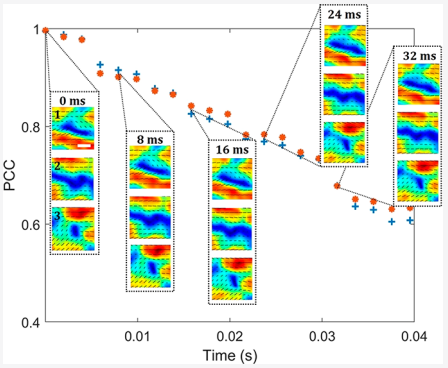

KEYWORDS: *polarization microscopy, single-shot imaging, birefringent structure*

Many materials, including liquid crystals (LCs),[1] collagen fibers,[2] and cytoskeletons,[3] are optically anisotropic. The structural anisotropy usually leads to refractive index anisotropy, termed birefringence. Polarization microscopes are powerful imaging tools to study these birefringent materials,[4] since they can visualize the birefringent structures by detecting the light components in different polarization directions. One of the most commonly used polarization microscopy techniques for characterizing molecular orientational conformation in birefringent specimens is fluorescence polarization-resolved microscopy,[5,6] which is based on doping the material with anisometric fluorescent dye molecules that report on the surrounding molecular director field.[5,7] This fluorescence approach can provide high-contrast and high-resolution imaging of birefringent structures but suffers from several shortcomings. The addition of fluorescent agents may affect the behavior of the underlying molecular matrix unless the doping concentration is very low. The imaging speed and the observation time are limited by the concentration and photobleaching of the fluorescent agents. Finally, implementing fluorescence approaches with confocal detection[7] or light-sheet microscopy[8,9] enables mapping of the molecular director field in three dimensions, however, raster or depth scanning approaches further limit the imaging speed to a few frames per second.[7,10,11] Although recent approaches have achieved millisecond temporal resolution,[12,13] these advances in imaging speed come at a cost of more complicated instrumentation with decreased applicability in studies of birefringent structure dynamics.

As a label-free alternative, conventional polarized light microscopy (PLM),[14] based on crossing a polarizer and an analyzer before and after the specimen, is often used for the imaging of the underlying molecular assembly in birefringent materials. PLM has found applications in studying flow-rate-dependent liquid crystal conformational profiles,[15,16] analyzing collagen fibers' architectures,[2] or measuring the photoelasticity of glass.[17] While qualitative polarization imaging with PLM has been broadly employed, quantitative polarization imaging is important for investigations of optically anisotropic materials. Stokes vectors,[18,19] Jones matrix,[20,21] and their associated polarization parameters have been used to quantitatively describe optical anisotropy. Among all of these polarization parameters, retardance and orientation angle are the two essential ones that are typically used for quantifying the properties and structures of birefringent specimens[14] with

Received: May 27, 2021
Published: November 17, 2021

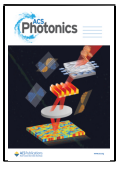

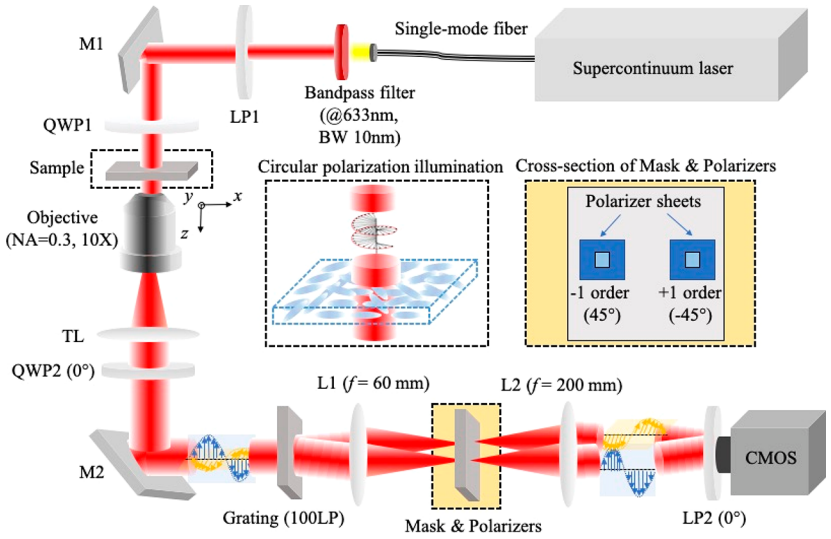

Figure 1. System design of polarized shearing interference microscopy. LP1 and LP2, linear polarizers; M1 and M2, mirrors; QWP1 and QWP2, quarter wave plates; TL, tube lens; L1 and L2, lenses. The z-axis is the direction of the optical axis, and the $x-y$ plane is the sample plane. The zoomed region denotes the circular polarization illumination and the location of the masks and polarizer sheets on the Fourier plane. After QWP2, the laser beams' polarization directions are shown with cartoon insets in the beams.

weak scattering and negligible absorption, such as a thin layer of tendon or liquid crystals. To resolve these two polarization parameters quantitatively, multiple measurements based on mechanical rotations of the polarizer and analyzer are needed[14] in conventional PLM, which is often too slow to study the dynamics of birefringent materials. To overcome these limitations, the LC-Polscope[22,23] has been developed that improved the accuracy, sensitivity, and speed of quantitative polarization imaging by replacing the compensators in conventional PLM with faster electro-optical LC universal retarders.[4,24,25] These improvements make the LC-Polscope a powerful tool for studying biological processes such as microtubule reorganization during cell mitosis[26,27] or dynamical events of birefringent samples such as LC flows,[28] but the imaging speed remains restricted by the requirement of multiple measurements to reconstruct the retardance and orientation angle maps.

To explore fast dynamics in birefringent structures, several high-speed quantitative polarization imaging techniques have been developed. Single-shot quantitative imaging of anisotropic sample's Stokes vectors[18,19] has been realized by adopting polarization cameras.[29,30] Alternatively, high-speed polarization imaging techniques combining polarization light microscopy with digital holographic microscopy[6,21,31,32] reduced the number of image acquisitions for quantitative retrieval of the polarization parameters. Furthermore, single-shot quantitative imaging of the samples' Jones matrix has been reported.[33,34] Several years ago, we reported a single-shot quantitative polarization imaging technique utilizing shearing interferometry[35] that can recover the anisotropic samples' retardance and orientation angle maps simultaneously. However, the Wollaston prism used in this system severely limits the image field-of-view (FOV) to a narrow rectangle. The use of Wollaston prisms further requires low numerical aperture objectives that reduces the spatial resolution. Moreover, the retardance and orientation angle retrieval algorithm amplifies the measurement noise and deteriorates the imaging sensitivity. Hindered by these limitations, this single-shot quantitative polarization imaging method is still not suitable for studying dynamics of birefringent samples with complex structures.

Here, we propose polarized shearing interference microscopy (PSIM) that overcomes all these limitations. We utilize a diffraction grating with polarizer sheets in the Fourier plane instead of a Wollaston prism, which enables single-shot quantitative polarization imaging with large FOV imaging (up to 350 × 350 μm^2) and high spatial resolution (~2 μm). An improved polarization parameter retrieval algorithm is developed that avoids noise amplification and improves the sensitivity when simultaneously recovering the retardance and orientation angle of the samples. The introduction of a supercontinuum laser source reduces image speckle noise, and the use of a fast Complementary Metal Oxide Semiconductor (CMOS) camera improves the acquisition speed. We show the capabilities of PSIM by imaging the flow of a lyotropic chromonic liquid crystal (LCLC) in a microfluidic channel at an imaging speed of 506 fps. We demonstrate that the evolution of the retardance and orientational angle maps of the flowing LCLC can be quantified with PSIM.

TECHNIQUE

Polarized Shearing Interference Microscopy (PSIM). A supercontinuum laser (Fianium SC-400) generates a broadband, spatially uniform illumination beam that is coupled to a single-mode optical fiber, as shown in Figure 1. The beam is collimated and transmits through a bandpass filter centered at 633 nm with a 10 nm bandwidth. A linear polarizer (LP1) and a quarter wave plate (QWP1) are crossed at an angle of 45° to generate a circularly polarized illumination. The scattered light is collected by an objective (Olympus UPLFLN10 × 2, NA = 0.3, 10×) and collimated by a tube lens (TL). The beam, which bears the polarization information on the sample, transmits through another quarter wave plate (QWP2), and is then separated into multiple orders by a 100 line-pair per millimeter (LP) diffraction grating. The grating is positioned at the conjugated plane of the sample plane. A 4f system is positioned after the diffraction grating to relay the beams. On the Fourier plane, a mask is placed that lets only the +1st order

https://doi.org/10.1021/acsphotonics.1c00788
ACS Photonics 2021, 8, 3440−3447

and -1^{st} order beams pass. Two polarizer sheets are placed on the mask: For the $+1^{st}$ order, the direction of the polarization sheet is 45° to the slow axis of QWP2, for the -1^{st} order, the direction of the polarization sheet is −45° to the slow axis of QWP2. Another linear polarizer (LP2) with polarization direction 45° to both polarizer sheets (0° to the slow axis of QWP2) is placed in front of the camera to produce interference between the two orders. The interferogram is recorded by a CMOS camera (Optronics CP80-4-M-500, full frame 2304 × 1720 pixels, pixel size 7 × 7 μm^2), whose maximum frame rate is 506 frames per second (fps). The imaging speed of PSIM is limited only by the camera frame rate.

Polarization Retrieval Algorithm. We have developed a new algorithm based on digital holography to quantitatively retrieve the 2D polarization parameters of birefringent samples. We recover the phase retardance and orientation angle of the samples directly by assuming the scattering of the sample is weak. This assumption is applicable for optically thin materials, where the retardance is directly related to the sample's birefringence rather than described by more complex Jones matrix components. Although this assumption may not be applicable for complex anisotropic samples, such as thick biological tissues or liquid crystal droplets, it allows for a significant simplification that enables the retardance and orientation angle to be measured in a single shot. To demonstrate this algorithm, we recover the polarization parameters of a crystallized Orange II fiber from its interferogram, as shown in Figure 2a. In the interferogram, fringes appear only in regions with high birefringence. We perform a two-dimensional Fourier transform to the interferogram and show the logarithm of the 2D spectrum in decibels (dB), as shown in Figure 2b, which reveals three orders on the Fourier domain (-1^{st}, 0^{th}, and $+1^{st}$ order). By extracting the $+1^{st}$ order with a circular linear filter and shifting it to the center of the Fourier plane, we can map the amplitude E and the phase φ of the light field after an inverse Fourier transform. The 0^{th} order gives access to the amplitude of the direct current (DC) term A. The retardance Δ can be calculated as

$$\Delta = \sin^{-1}\left(\frac{2E}{A}\right) \tag{1}$$

and the distribution of the orientation angle ϕ is calculated as

$$\varphi = \frac{1}{2}\phi \tag{2}$$

The retardance Δ and the orientation angle ϕ distributions are decoupled into the measured amplitude E and the measured phase φ, respectively, as shown in Figure 2c,d. The derivation of the polarization parameter retrieval and the preparation of the Orange II samples are discussed in the Methods section. The calibration approaches used to eliminate the background noise and to improve the imaging accuracy are elaborated in the Supporting Information.

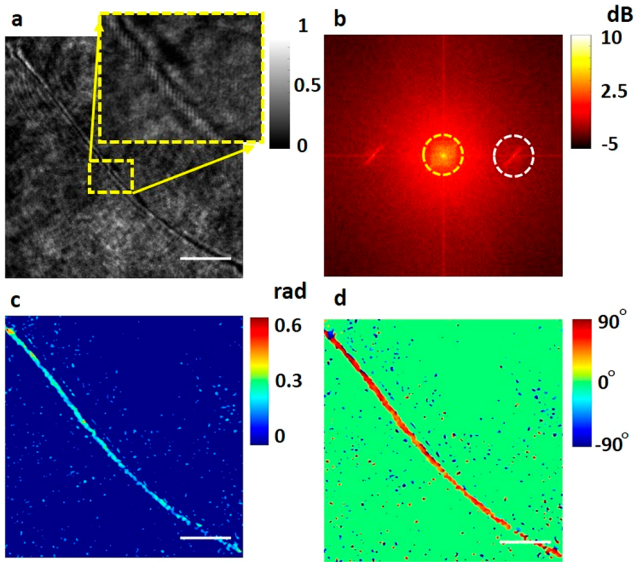

Figure 2. Demonstration of the polarization parameter retrieval algorithm. (a) Interferogram of a crystal fiber sample. The zoomed region denotes the fiber region with a high birefringence signal. (b) Logarithm map of the Fourier domain of (a), reported in decibels (dB), where the 0^{th} and $+1^{st}$ orders are labeled with yellow and white circles, respectively. (c) Quantitative map of the retardance distribution. (d) Quantitative map of the orientation angle distribution. The scale bars denote 20 μm.

RESULTS

Validation of PSIM's Measurement Accuracy Using a Birefringence Target. The retardance and orientation angle of a birefringent resolution target (R2L2S1B, Thorlabs) are quantitively mapped to validate the measurement accuracy of PSIM, as shown in Figure 3a. Since the features in the birefringent resolution target are larger than liquid crystal fibers and bovine tendon samples, we use a 4×/0.16 objective (UPLXAPO4X, Olympus) to enlarge the field-of-view to 1 mm × 1 mm. Based on the manufacturer's specification, the retardance is uniform across the entire target, and its absolute value is 280 ± 20 nm, which corresponds to 2.78 ± 0.20 rad under our illumination wavelength of 633 nm. Since the range of measurable retardance values of PSIM is between 0 and $\pi/2 \approx 1.57$, the ground truth retardance value of the birefringent resolution target is 0.36 ± 0.20 rad for the PSIM system. From Figure 3a, we calculate the mean value of the measured retardance map, which is 0.44 rad, with a standard deviation of 0.05 rad over the entire field-of-view. For the orientation angle, the patterned regions have different values from the background. The mean orientation angle of the patterned region (purple dashed box in Figure 3b) is 32.87° with a standard deviation of 2.67°. For the background region (green dashed box in Figure 3b), the mean orientation angle is −1.49°, with a standard deviation of 2.63°. As a further validation, we perform the measurements using conventional quantitative polarization light microscopy (PLM) for the same birefringence resolution target. In PLM, the retardance map has a mean value of 0.48 rad with a spatial standard deviation of 0.03 rad, the patterned region has a mean orientation angle value of 30.31° with a standard deviation of 2.24°, and the orientation angle value range in the background has a mean value of −1.23° and a standard deviation of 3.05°. The comparison of PLM and PSIM is elaborated in the Supporting Information.

Validation of PSIM's Measurement Accuracy for Complex Birefringent Structures Using a Rotating Bovine Tendon Specimen. The retardance and orientation angle of a bovine tendon specimen are quantitatively mapped and evaluated at different rotation angles, as shown in Figure 3c−e. The bovine tendons are sliced into specimens of a thickness of 5 μm, sandwiched between a glass slide and a

https://doi.org/10.1021/acsphotonics.1c00788
ACS Photonics 2021, 8, 3440−3447

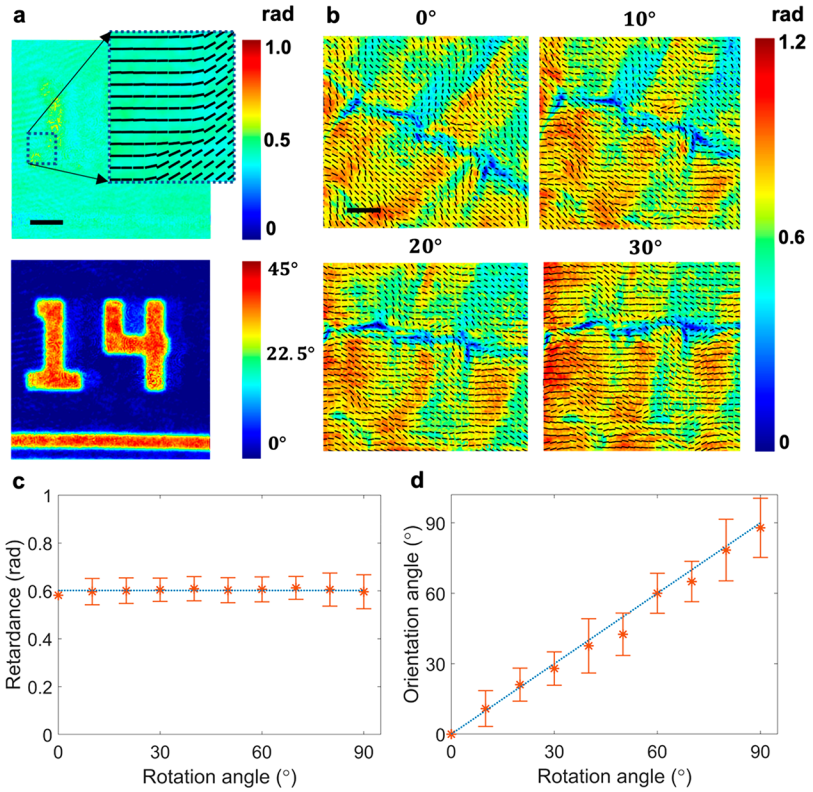

Figure 3. Validation of the imaging concept. The (a) retardance and (b) orientation angle maps of the birefringence target. We zoom into a small region at the boundary of the pattern. The combination of the retardance map and the orientation angle's quiver plot of this region is shown as a subfigure. The scale bar is 200 μm. (c) Combination of the retardance map and orientation angle quiver plot of the bovine tendon specimen, for rotation angles of 0°, 10°, 20°, and 30°. The scale bar denotes 25 μm. (d) Averaged retardance and (e) orientation angle vs the rotation angle. The red asterisks denote the average values, the error bars denote the standard deviations over the field-of-view. The blue dashed lines denote the averaged values of retardance and rotation angles, respectively.

coverslip, and fixed on the rotation stage (Thorlabs, OCT-XYR1/M) with clippers. The bovine tendon contains abundant collagen fibers with a large birefringence. The orientation of the fibers in the tendon are relatively uniform, except for small undulations. The tendon sample is an example of an anisotropic material with a complex morphology, which makes it ideal for validating the measurement accuracy and imaging performance of PSIM. A bovine tendon specimen is imaged at rotation angles from 0° to 90° at increments of 10°. The retardance and orientation angle maps are retrieved at each rotation angle. Since the field-of-view at different rotation angles slightly shifts upon rotation, an image registration method (reported in the Supporting Information) is used to find the most correlated regions in the retardance images at adjacent rotation angles. Maps of the polarization parameters of the most correlated regions at rotation angles of 0°, 10°, 20°, and 30° are shown in Figure 3c, where each image combines the retardance images and the quiver plots of orientation angles. The direction of the rods in the quiver plots indicate that the orientation angle follows the undulation of the fibrous structures seen in the retardance images.

We further validate that the spatial average of the retrieved retardance maps remains constant, while the average values of the orientation angle maps match the rotation angles when we rotate the sample. The spatial averaged values and standard deviations of the retardance and orientation angle in the most correlated region found with our image registration algorithm are shown as functions of the rotation angle in Figure 3d,e. For the retardance, the mean of the spatially averaged values over all the rotation angles is 0.60 rad, with a standard deviation of 0.01 rad, which indicates that the change in mean retardance is negligible as we rotate the sample stage. The spatial standard deviation of the retardance difference maps between adjacent rotation angles is 0.05 rad, indicating that the pixel mismatch caused by our image registration algorithm is negligible. For the orientation angle, the mean error between the averaged orientation angles and rotation angles is 2.39°, indicating that the orientation angle measurement with PSIM is accurate even for complex birefringent structures. The spatial standard deviation of the orientation angle difference between two adjacent rotation angles is 9.47°. This value is slightly larger than the spatial uncertainty of the retardance, partly due to the orientation angle being more sensitive to the mismatch of the tendon's fibrous structure. To avoid the inaccuracy introduced by the error of the mechanical rotation of the sample stage, the rotation angles are also determined by an image registration algorithm (details are reported in the Supporting Information).

Quantitative Polarization Imaging of Liquid Crystal Flows. Lyotropic chromonic liquid crystals (LCLCs) are biocompatible water-based materials composed of self-assembled cylindrical aggregates.[36−39] They are promising candidates for controlling assembly of particles and biomaterials in microfluidic channels,[40−42] but their flow properties are currently poorly understood,[42−44] partly due to the lack of quantitative polarization imaging methods with fast enough imaging speeds that allow investigations of LCLCs at high flow rate.[28] We apply PSIM to quantitatively image the flow of aqueous solutions of the LCLC disodium cromoglycate

https://doi.org/10.1021/acsphotonics.1c00788
ACS Photonics 2021, 8, 3440−3447

(DSCG) in a microfluidic channel. The director field of the liquid crystal is three-dimensional (3D), varying across the channel thickness.[44] Our two-dimensional (2D) technique provides the integrated retardance and orientation angle across the thickness, which can then be validated with and compared to simulations that can provide access to the 3D director field.[44] The retardance Δ measured in PSIM is the integrated phase difference between the projected extraordinary and ordinary axes of the liquid crystal, and the angle ϕ denotes the in-plane orientation angle averaged along the channel thickness direction, which describes the director orientation in the $x-y$ plane, as shown in Figure 4a.

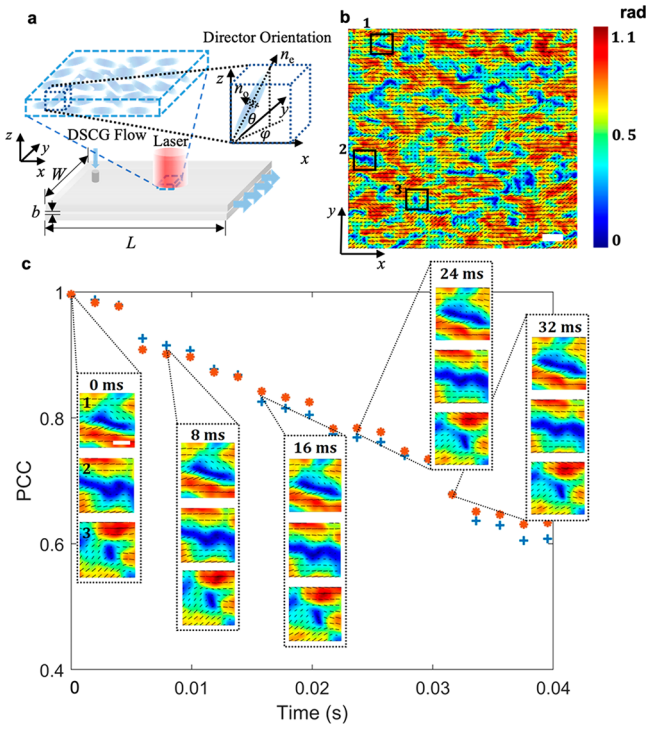

Figure 4. Temporal evolution of the retardance and orientation angle maps of a flowing liquid crystal. (a) Schematics of the microfluidic channel of length L = 50 mm, width W = 15 mm, and thickness b = 6.5 μm used to probe the flow of a nematic DSCG solution, and of the director orientation. (b) Retardance and orientation angle maps for a flow rate of 1 μL/min. The color and the length of the rods represent the magnitude of retardance, the direction of the rods denotes the orientation angle. The three regions of size 100 × 100 pixels discussed in (c) are indicated. The flow is in the x-direction. (c) Temporal evolution of the Pearson Correlation Coefficient (PCC) of the retardance (blue plus signs) and orientation angle (red asterisks) maps and snapshots of the three selected regions. The scale bars in (b) and (c) denote 20 and 10 μm, respectively.

The microfluidic channel used in our study is shown in Figure 4a. We control the initial conditions by injecting aqueous solutions of 13 wt % DSCG into the channel and allowing the solutions to relax on rubbed surfaces where the directors are aligned along the flow direction (x-direction). We start the flow at a flow rate of 1 μL/min controlled by a syringe pump (Harvard PHD 2000). When the flow has reached a steady state, we image the sample in a 252 × 252 μm^2 region at an imaging speed of 506 fps.

We retrieve the retardance and orientation angle maps for each frame of the video (see Supporting Information, Videos 1, 2, and 3). The color map of the retardance and the quiver plot of the orientation angle are shown in Figure 4b. The colors and the length of the rods represent the magnitude of retardance, and the direction of the rods denotes the orientation angle. Note that the birefringence of a 13 wt % DSCG solution is $n_e - n_0 \approx -0.015$ at a wavelength of 633 nm,[45,46] where n_e and n_0 are the extraordinary and ordinary refractive indices, respectively. The birefringence leads to a maximum retardance of ~0.98 ± 0.15 rad, well within the maximum measurable value $\pi/2$ of PSIM. Complex structures appear in the flow of DSCG: low retardance regions of well-defined size emerge in the steady-state flow.

Tracking the Temporal Evolution of the Retardance and Orientation Angle. The spatial distribution of the retardance and orientation angle maps of DSCG solutions at shear rates below 10 s^{-1} have recently been studied using a LC-Polscope.[28] Thanks to the large field-of-view and the high imaging speed of PSIM, we can quantify the spatiotemporal dynamics of the structures that emerge in the flow.[44] We focus on the selected low-retardance regions of a window size of 100 × 100 pixels, as shown in Figure 4b, and track their evolution over time. We quantify the temporal evolution of the retardance and orientation angle by calculating the Pearson Correlation Coefficient (PCC) for time intervals of 2 ms, as shown in Figure 4c (details of the analysis and the time-lapse videos of the polarization parameters of the selected regions are provided in the Supporting Information). The PCC values for both the retardance and the orientation angle monotonically decrease with time, indicating the motion of the structures.

DISCUSSION AND CONCLUSIONS

For the study of thin, nonabsorbing specimens, such as liquid crystals in microfluidic devices, PSIM offers significant simplifications in the design of the polarization imaging apparatus and the parameter retrieval algorithms compared to other single-shot polarization imaging techniques.[18,19,33,34] Focusing on the extraction of the specimen's retardance and orientation angle distribution, we have developed an efficient parameter retrieval algorithm for high-speed imaging using a simple, low-cost instrument. The recent progress in this field can be separated into two groups: The first group[18,19] realizes single-shot polarization imaging using polarization cameras, where pixels within a cluster have different polarization filters to enable single-shot acquisition of the full Jones matrix or Stokes vector. While this approach is fast and provides a comprehensive measurement of the Jones matrix components, its need for a specialized camera may be a significant hurdle for adoption. The second group[6,21,31−34] combines polarization-sensitive microscopy with a noncommon path, off-axis interferometry to reduce the number of measurements needed for polarization parameter retrieval. Such noncommon-path approaches, however, generally have lower sensitivity and are more susceptible to mechanical perturbations. These issues can be mitigated by using near-common-path interferometric microscopy systems in polarization imaging,[47] which is also adopted in our PSIM. However, to the best of our knowledge, these prior works do not realize single-shot quantitative polarization imaging, as they acquire more comprehensive Jones matrix information, while we focus on the retardance and orientation angle that fully characterize the polarization state of our type of specimens. PSIM thus offers a novel, high-stability, high-resolution (~2 μm), large field-of-view (350 × 350 μm^2),

https://doi.org/10.1021/acsphotonics.1c00788
ACS Photonics 2021, 8, 3440−3447

and cost-effective approach that is suitable for monitoring polarization states of thin, nonabsorbing specimen at unprecedented frame rates (~500 fps). We have validated that the retardance and orientation angle can be accurately measured when imaging birefringent resolution targets, and we demonstrate that PSIM can resolve the orientation change and the spatial undulations of bovine tendon fibers with high accuracy when imaging rotating specimens. PSIM allows us to quantify the fast dynamics of a nematic lyotropic chromonic liquid crystal flowing in a microfluidic channel and to track the emerging structures. Enabling high-speed quantitative polarization imaging, PSIM opens the path for quantifying and interpreting the dynamics of liquid crystals and other birefringent materials.

METHODS

Derivation of the Polarization Retrieval Algorithm. We use Jones calculus[48] to derive the polarization retrieval algorithm for PSIM. Different from previous studies[49,50] that retrieve both amplitude and phase information on each component of the Jones matrix, we assume each component of the sample's Jones matrix is "only phase" (i.e., the amplitude is uniform). This assumption is valid for samples with weak scattering and negligible absorption, such as liquid crystals and thin biological tissue slices. In eq 3, we formulate the Jones matrix of the "only phase" sample and relate it to the retardance and orientation angle:

$$J_{\text{sample}} = \begin{pmatrix} \cos\varphi & \sin\varphi \\ -\sin\varphi & \cos\varphi \end{pmatrix}\begin{pmatrix} e^{j\phi_e} & 0 \\ 0 & e^{j\phi_o} \end{pmatrix}\begin{pmatrix} \cos\varphi & -\sin\varphi \\ \sin\varphi & \cos\varphi \end{pmatrix}$$
$$= \begin{pmatrix} e^{i\phi_e}\cos^2\varphi + e^{i\phi_o}\sin^2\varphi & -(e^{i\phi_e} - e^{i\phi_o})\sin\varphi\cos\varphi \\ -(e^{i\phi_e} - e^{i\phi_o})\sin\varphi\cos\varphi & e^{i\phi_e}\sin^2\varphi + e^{i\phi_o}\cos^2\varphi \end{pmatrix} \quad (3)$$

where ϕ_e is the phase delay in the extraordinary axis of the birefringent sample, ϕ_o is the phase delay in the ordinary axis, and ϕ is the orientation angle. The retardance Δ is the difference between the phase delay in the extraordinary axis and that in the ordinary axis, $\Delta = \phi_e - \phi_o$. These parameters are mapped in real space, and the notations for Cartesian coordinates (x, y) are omitted for clarity. We utilize a linear polarizer (LP1) and a quarter wave plate (QWP1) to generate a left-handed circular polarization illumination:

$$E_{\text{in}} = \frac{1}{\sqrt{2}}\begin{pmatrix} 1 \\ i \end{pmatrix} \quad (4)$$

After the beam is transmitted through the sample, the scattered light is collected by an objective and passes through another quarter wave plate (QWP2). The output field is

$$E_{\text{out}} = e^{i\pi/4}\begin{pmatrix} 1 & 0 \\ 0 & i \end{pmatrix}J_{\text{sample}}E_{\text{in}}$$
$$= \frac{1}{\sqrt{2}}e^{i\pi/4}\begin{pmatrix} e^{i\phi_e}(\cos^2\varphi - i\sin\varphi\cos\varphi) + e^{i\phi_o}(\sin^2\varphi + i\sin\varphi\cos\varphi) \\ e^{i\phi_e}(-\sin^2\varphi - i\sin\varphi\cos\varphi) + e^{i\phi_o}(-\cos^2\varphi + i\sin\varphi\cos\varphi) \end{pmatrix} \quad (5)$$

Subsequently, the light is separated by a diffraction grating. Only the +1 and −1 orders of the light pass through the Fourier plane. After a polarizer with orientation direction of 45° to the slow axis of QWP2, an output field is produced:

$$E_{\text{out},45^\circ} = \frac{1}{2}e^{i\pi/4}(e^{i\phi_e} - e^{i\phi_o})\exp(-i2\varphi)$$
$$= \sin\frac{\Delta}{2}\exp\left[i\left(\frac{\phi_e + \phi_o}{2} - 2\varphi + \frac{3\pi}{4}\right)\right] \quad (6)$$

Note that the retardance is only contained in the amplitude part and the orientation angle is only contained in the phase part. However, the presence of an average phase delay $(\frac{\phi_e + \phi_o}{2})$ prevents the retrieval of the orientation angle. The output electric field for a linear polarizer set to −45° to the slow axis of QWP2 is expressed as

$$E_{\text{out},-45^\circ} = \frac{1}{2}e^{i\pi/4}(e^{i\phi_e} + e^{i\phi_o}) = \cos\frac{\Delta}{2}\exp\left[i\left(\frac{\phi_e + \phi_o}{2} + \frac{\pi}{4}\right)\right] \quad (7)$$

The orientation angle contained in the phase part disappears, and only the average phase delay remains. This offers a strategy to cancel out the average phase delay. Two perpendicularly oriented polarizers are placed on the Fourier plane to generate these two output fields simultaneously: one is in the $+1^{\text{st}}$ order and the other is in the -1^{st} order:

$$E_{+1} = \sin\frac{\Delta}{2}\exp\left[i\left(\frac{\phi_e + \phi_o}{2} - 2\varphi + \frac{3\pi}{4} + \frac{kx}{2}\right)\right] \quad (8)$$

and

$$E_{-1} = \cos\frac{\Delta}{2}\exp\left[i\left(\frac{\phi_e + \phi_o}{2} + \frac{\pi}{4} - \frac{kx}{2}\right)\right] \quad (9)$$

kx denotes the spatial modulation caused by the separation of the diffraction grating. A second polarizer (LP2) with orientation 45° to both polarizers on the Fourier plane is used to produce interference, and an interferogram is recorded by a CMOS camera:

$$I = \langle(E_{+1} + E_{-1})(E_{+1} + E_{-1})^*\rangle$$
$$= |E_{+1}|^2 + |E_{-1}|^2 + \langle E_{+1}E_{-1}^*\rangle + \langle E_{-1}E_{+1}^*\rangle$$
$$= \sin^2\frac{\Delta}{2} + \cos^2\frac{\Delta}{2} + 2\sin\frac{\Delta}{2}\cos\frac{\Delta}{2}\cos\left[\left(\frac{\phi_e + \phi_o}{2} - 2\varphi + \frac{3\pi}{4}\right) - \left(\frac{\phi_e + \phi_o}{2} + \frac{\pi}{4}\right) + kx\right]$$
$$= 1 + \sin\Delta\sin(2\varphi - kx) \quad (10)$$

By retrieving the complex field in the alternating current (AC) term, we calculate the retardance and orientation angle distribution, eqs 1 and 2.

Sample Preparation. Orange II is purchased from Sigma-Aldrich, and aqueous solutions with weight concentration c = 35.0 wt % are prepared in the nematic phase.

Bovine tendon is purchased at a local market. After cutting the tendon samples with a scalpel, they are stored in 10% formalin (Sigma-Aldrich) for at least 72 h. Subsequently, the samples are dehydrated in ethanol and embedded in paraffin to fix the thin sections to be imaged.

Disodium cromoglycate (DSCG) is purchased from TCI America (purity > 98.0%). The DSCG is dissolved in deionized water at a concentration of c = 13.0 wt %.[51] The microfluidic channel consists of two rectangular glass plates separated by 6.5 ± 1 μm spacers (Specac, MY SPR RECT 0.006 mm OMNI). We use diamond particles of diameter ~50

https://doi.org/10.1021/acsphotonics.1c00788
ACS Photonics 2021, 8, 3440−3447

nm to rub both glass plates along the channel length direction, which induces uniform planar alignment.

■ ASSOCIATED CONTENT

Supporting Information

The Supporting Information is available free of charge at https://pubs.acs.org/doi/10.1021/acsphotonics.1c00788.

A description of the validation of PSIM's measurement accuracy using a rotating wave plate; a comparison of imaging results of PSIM and conventional Polarization Light Microscopy (PLM); an analysis of the temporal sensitivity and spatial sensitivity; the calibration procedure for the retrieved parameters; a description of the image registration method; a visualization of the retrieved parameters via tracking the temporal evolution of patterns emerging in flowing DSCG solutions (PDF)

Visualization of the emerging patterns in flowing DSCG Video 1: The quiver plot of a selected low retardance region's change(AVI)

Visualization of the emerging patterns in flowing DSCG Video 2: The tracking of a selected low-retardance region (AVI)

Visualization of the emerging patterns in flowing DSCG Video 3: The quiver plot of the DSCG flow within the entire field-of-view(AVI)

■ AUTHOR INFORMATION

Corresponding Author

Peter T. C. So − *Department of Mechanical Engineering, Massachusetts Institute of Technology, Cambridge, Massachusetts 02139, United States; Laser Biomedical Research Center and Department of Biological Engineering, Massachusetts Institute of Technology, Cambridge, Massachusetts 02139, United States*; Email: ptso@mit.edu

Authors

Baoliang Ge − *Department of Mechanical Engineering, Massachusetts Institute of Technology, Cambridge, Massachusetts 02139, United States; Laser Biomedical Research Center, Massachusetts Institute of Technology, Cambridge, Massachusetts 02139, United States;* orcid.org/0000-0002-1792-8871

Qing Zhang − *Department of Mechanical Engineering, Massachusetts Institute of Technology, Cambridge, Massachusetts 02139, United States*

Rui Zhang − *Department of Physics, The Hong Kong University of Science and Technology, Hong Kong 999077, China*

Jing-Tang Lin − *Department of Physics, National Taiwan University, Taipei 106 Taiwan, Republic of China*

Po-Hang Tseng − *Department of Physics, National Taiwan University, Taipei 106 Taiwan, Republic of China*

Che-Wei Chang − *Department of Physics, National Taiwan University, Taipei 106 Taiwan, Republic of China*

Chen-Yuan Dong − *Department of Physics, National Taiwan University, Taipei 106 Taiwan, Republic of China*

Renjie Zhou − *Department of Biomedical Engineering, The Chinese University of Hong Kong, New Territories, Hong Kong 999077, China;* orcid.org/0000-0002-4761-6641

Zahid Yaqoob − *Laser Biomedical Research Center, Massachusetts Institute of Technology, Cambridge, Massachusetts 02139, United States*

Irmgard Bischofberger − *Department of Mechanical Engineering, Massachusetts Institute of Technology, Cambridge, Massachusetts 02139, United States*

Complete contact information is available at: https://pubs.acs.org/10.1021/acsphotonics.1c00788

Author Contributions

#These authors contributed equally to this work.

Notes

The authors declare no competing financial interest.

■ ACKNOWLEDGMENTS

B.G., Z.Y., and P.T.C.S. acknowledge support from the National Institutes of Health (NIH) 5-P41-EB015871-27 and 5R21NS091982-02, and the Hamamatsu Corporation. B.G. and P.T.C.S. acknowledge support from the Singapore−MIT Alliance for Research and Technology (SMART) Center, Critical Analytics for Manufacturing Personalized-Medicine IRG. B.G. acknowledges support from MathWorks Fellowship. Q.Z. and I.B. acknowledge support from the MIT Research Support Committee. Z.Y. and P.T.C.S. acknowledge support from NIH R01DA045549 and R21GM140613-02. R.Z. acknowledges support from the Hong Kong RGC Grant No. 26302320. R.Z. acknowledges the Croucher Foundation (Award Number: CM/CT/CF/CIA/0688/19ay). C.Y.D., J.T.L., P.H.T., and C.W.C. acknowledge 107-2112-M-002-023-MY3, Ministry of Science and Technology, Taiwan, R.O.C.

■ REFERENCES

(1) Yang, D. K.; Wu, S. T. *Fundamentals of Liquid Crystal Devices*; John Wiley & Sons, 2014, DOI: 10.1002/9781118751992.

(2) Yang, B.; Jan, N. J.; Brazile, B.; Voorhees, A.; Lathrop, K. L.; Sigal, I. A. Polarized Light Microscopy for 3-Dimensional Mapping of Collagen Fiber Architecture in Ocular Tissues. *J. Biophotonics* **2018**, *11* (8), 1−11.

(3) Mehta, S. B.; McQuilken, M.; La Riviere, P. J.; Occhipinti, P.; Verma, A.; Oldenbourg, R.; Gladfelter, A. S.; Tani, T. Dissection of Molecular Assembly Dynamics by Tracking Orientation and Position of Single Molecules in Live Cells. *Proc. Natl. Acad. Sci. U. S. A.* **2016**, *113* (42), E6352−E6361.

(4) Oldenbourg, R. Polarized Light Microscopy: Principles and Practice. *Cold Spring Harb. Protoc.* **2013**, *2013* (11), 1023−1036.

(5) Smalyukh, I. I.; Shiyanovskii, S. V.; Lavrentovich, O. D. Three-Dimensional Imaging of Orientational Order by Fluorescence Confocal Polarizing Microscopy. *Chem. Phys. Lett.* **2001**, *336* (1−2), 88−96.

(6) Lee, T.; Senyuk, B.; Trivedi, R. P.; Smalyukh, I. I. Optical Microscopy of Soft Matter Systems. *Fluids, Colloids and Soft Materiels: An Introduction to Soft Matter Physics*; Wiley, 2018; Vol *20*, Iss 9, pp 165−186,

(7) Lavrentovich, O. D. Fluorescence Confocal Polarizing Microscopy: Three-Dimensional Imaging of the Director. *Pramana* **2003**, *61* (2), 373−384.

(8) Kim, T.; Zhou, R.; Mir, M.; Babacan, S. D.; Carney, P. S.; Goddard, L. L.; Popescu, G. White-Light Diffraction Tomography of Unlabelled Live Cells. *Nat. Photonics* **2014**, *8* (3), 256−263.

(9) Duclos, G.; Adkins, R.; Banerjee, D.; Peterson, M. S. E.; Varghese, M.; Kolvin, I.; Baskaran, A.; Pelcovits, R. A.; Powers, T. R.; Baskaran, A.; Toschi, F.; Hagan, M. F.; Streichan, S. J.; Vitelli, V.; Beller, D. A.; Dogic, Z. Topological Structure and Dynamics of Three-Dimensional Active Nematics. *Science* **2020**, *367* (6482), 1120−1124.

(10) Wolleschensky, R.; Zimmermann, B.; Kempe, M. High-Speed Confocal Fluorescence Imaging with a Novel Line Scanning Microscope. *J. Biomed. Opt.* **2006**, *11* (6), 064011.

(11) Wang, Q.; Zheng, J.; Wang, K.; Gui, K.; Guo, H.; Zhuang, S. Parallel Detection Experiment of Fluorescence Confocal Microscopy Using DMD. *Scanning* **2016**, *38* (3), 234−239.
(12) Stehbens, S.; Pemble, H.; Murrow, L.; Wittmann, T. Imaging Intracellular Protein Dynamics by Spinning Disk Confocal Microscopy. *Methods in Enzymology*; Elsevier Inc., 2012; Vol. *504*, pp 293−313, DOI: 10.1016/B978-0-12-391857-4.00015-X.
(13) Singh, V. R.; Yang, Y. A.; Yu, H.; Kamm, R. D.; Yaqoob, Z.; So, P. T. C. Studying Nucleic Envelope and Plasma Membrane Mechanics of Eukaryotic Cells Using Confocal Reflectance Interferometric Microscopy. *Nat. Commun.* **2019**, *10* (1), 1−8.
(14) Oldenbourg, R. Polarized Light Microscopy: Principles and Practice. *Cold Spring Harb. Protoc.* **2013**, *2013* (11), 1023−1036.
(15) Sengupta, A.; Schulz, B.; Ouskova, E.; Bahr, C. Functionalization of Microfluidic Devices for Investigation of Liquid Crystal Flows. *Microfluid. Nanofluid.* **2012**, *13* (6), 941−955.
(16) Sengupta, A.; Tkalec, U.; Ravnik, M.; Yeomans, J. M.; Bahr, C.; Herminghaus, S. Liquid Crystal Microfluidics for Tunable Flow Shaping. *Phys. Rev. Lett.* **2013**, *110* (4), 1−5.
(17) Rodano, S. J.; D'Amario, J. J. Elasticity of Glass; The Physics Teacher. *Phys. Teach.* **1979**, *17*, 595.
(18) Tian, X.; Tu, X.; Della Croce, K.; Yao, G.; Cai, H.; Brock, N.; Pau, S.; Liang, R. Multi-Wavelength Quantitative Polarization and Phase Microscope. *Biomed. Opt. Express* **2019**, *10* (4), 1638.
(19) Tahara, T.; Awatsuji, Y.; Shimozato, Y.; Kakue, T.; Nishio, K.; Ura, S.; Kubota, T.; Matoba, O. Single-Shot Polarization-Imaging Digital Holography Based on Simultaneous Phase-Shifting Interferometry. *Opt. Lett.* **2011**, *36* (16), 3254.
(20) Colomb, T.; Dahlgren, P.; Beghuin, D.; Cuche, E.; Marquet, P.; Depeursinge, C. Polarization Imaging by Use of Digital Holography. *Appl. Opt.* **2002**, *41* (1), 27.
(21) Wang, Z.; Millet, L. J.; Gillette, M. U.; Popescu, G. Jones Phase Microscopy of Transparent and Anisotropic Samples. *Opt. Lett.* **2008**, *33* (11), 1270.
(22) Oldenbourg, R. Polarization Microscopy with the LC-PolScope. *Live Cell Imaging: A Laboratory Manual*; Cold Spring Harbor Laboratory Press, 2005; pp 205−237.
(23) Shribak, M. I.; Oldenbourg, R. Mapping Polymer Birefringence in 3D Using a Polarizing Microscope with Oblique Illumination. *Proc. SPIE* **2004**, *5462*, 57.
(24) Oldenbourg, R. A New View on Polarization Microscopy. *Nature* **1996**, *381* (6585), 811−812.
(25) Shribak, M.; Oldenbourg, R. Techniques for Fast and Sensitive Measurements of Two-Dimensional Birefringence Distributions. *Appl. Opt.* **2003**, *42* (16), 3009−3017.
(26) Inoué, S.; Oldenbourg, R. Microtubule Dynamics in Mitotic Spindle Displayed by Polarized Light Microscopy. *Mol. Biol. Cell* **1998**, *9* (July), 1603−1607.
(27) Oldenbourg, R.; Salmon, E. D.; Tran, P. T. Birefringence of Single and Bundled Microtubules. *Biophys. J.* **1998**, *74* (1), 645−654.
(28) Baza, H.; Turiv, T.; Li, B. X.; Li, R.; Yavitt, B. M.; Fukuto, M.; Lavrentovich, O. D. Shear-Induced Polydomain Structures of Nematic Lyotropic Chromonic Liquid Crystal Disodium Cromoglycate. *Soft Matter* **2020**, *16* (37), 8565−8576.
(29) Brock, N. J.; Millerd, J. E.; Wyant, J. C.; Hayes, J. B. Pixelated Phase-Mask Interferometer. U.S. Patent, 7230717, 2007.
(30) Onuma, T.; Otani, Y. A Development of Two-Dimensional Birefringence Distribution Measurement System with a Sampling Rate of 1.3 MHz. *Opt. Commun.* **2014**, *315*, 69−73.
(31) Colomb, T.; Dürr, F.; Cuche, E.; Marquet, P.; Limberger, H. G.; Salathé, R. P.; Depeursinge, C. Polarization Microscopy by Use of Digital Holography: Application to Optical-Fiber Birefringence Measurements. *Appl. Opt.* **2005**, *44* (21), 4461−4469.
(32) Shin, S.; Lee, K.; Yaqoob, Z.; So, P. T. C.; Park, Y. Reference-Free Polarization-Sensitive Quantitative Phase Imaging Using Single-Point Optical Phase Conjugation. *Opt. Express* **2018**, *26* (21), 26858.
(33) Liu, X.; Wang, B.-Y.; Guo, C.-S. One-Step Jones Matrix Polarization Holography for Extraction of Spatially Resolved Jones Matrix of Polarization-Sensitive Materials. *Opt. Lett.* **2014**, *39* (21), 6170.
(34) Yang, T. D.; Park, K.; Kang, Y. G.; Lee, K. J.; Kim, B.-M.; Choi, Y. Single-Shot Digital Holographic Microscopy for Quantifying a Spatially-Resolved Jones Matrix of Biological Specimens. *Opt. Express* **2016**, *24* (25), 29302.
(35) Ge, B.; Zhou, R.; Takiguchi, Y.; Yaqoob, Z.; So, P. T. C. Single-Shot Optical Anisotropy Imaging with Quantitative Polarization Interference Microscopy. *Laser Photonics Rev.* **2018**, *12* (8), 1800070.
(36) Shiyanovskii, S. V.; Lavrentovich, O. D.; Schneider, T.; Ishikawa, T.; Smalyukh, I. I.; Woolverton, C. J.; Niehaus, G. D.; Doane, K. J. Lyotropic Chromonic Liquid Crystals for Biological Sensing Applications. *Mol. Cryst. Liq. Cryst.* **2005**, *434*, 259−270.
(37) Tam-Chang, S. W.; Seo, W.; Rove, K.; Casey, S. M. Molecularly Designed Chromonic Liquid Crystals for the Fabrication of Broad Spectrum Polarizing Materials. *Chem. Mater.* **2004**, *16* (10), 1832−1834.
(38) Nazarenko, V. G.; Boiko, O. P.; Anisimov, M. I.; Kadashchuk, A. K.; Nastishin, Y. A.; Golovin, A. B.; Lavrentovich, O. D. Lyotropic Chromonic Liquid Crystal Semiconductors for Water-Solution Processable Organic Electronics. *Appl. Phys. Lett.* **2010**, *97* (26), 263305.
(39) Guo, F.; Mukhopadhyay, A.; Sheldon, B. W.; Hurt, R. H. Vertically Aligned Graphene Layer Arrays from Chromonic Liquid Crystal Precursors. *Adv. Mater.* **2011**, *23* (4), 508−513.
(40) Zhou, S.; Sokolov, A.; Lavrentovich, O. D.; Aranson, I. S. Living Liquid Crystals. *Proc. Natl. Acad. Sci. U. S. A.* **2014**, *111* (4), 1265−1270.
(41) Genkin, M. M.; Sokolov, A.; Lavrentovich, O. D.; Aranson, I. S. Topological Defects in a Living Nematic Ensnare Swimming Bacteria. *Phys. Rev. X* **2017**, *7* (1), 1−14.
(42) Zhou, S.; Tovkach, O.; Golovaty, D.; Sokolov, A.; Aranson, I. S.; Lavrentovich, O. D. Dynamic States of Swimming Bacteria in a Nematic Liquid Crystal Cell with Homeotropic Alignment. *New J. Phys.* **2017**, *19* (5), 055006.
(43) Sharma, A.; Ong, I. L. H.; Sengupta, A. Time Dependent Lyotropic Chromonic Textures in Microfluidic Confinements. *Crystals* **2021**, *11* (1), 35.
(44) Zhang, Q.; Zhang, R.; Ge, B.; Yaqoob, Z.; So, P. T. C.; Bischofberger, I. Structures and Topological Defects in Pressure-Driven Lyotropic Chromonic Liquid Crystals. *Proc. Natl. Acad. Sci. U. S. A.* **2021**, *118* (35), e2108361118.
(45) Nastishin, Y. A.; Liu, H.; Schneider, T.; Nazarenko, V.; Vasyuta, R.; Shiyanovskii, S. V.; Lavrentovich, O. D. Optical Characterization of the Nematic Lyotropic Chromonic Liquid Crystals: Light Absorption, Birefringence, and Scalar Order Parameter. *Phys. Rev. E - Stat. Nonlinear, Soft Matter Phys.* **2005**, *72* (4), 1−14.
(46) Varga, L. K.; Mazaleyrat, F.; Kovac, J.; Greneche, J. M. Structural and Magnetic Properties of Metastable Fe1-XSix ($0.15 < x < 0.34$) Alloys Prepared by a Rapid-Quenching Technique. *J. Phys.: Condens. Matter* **2002**, *14* (8), 1985−2000.
(47) Kim, Y.; Jeong, J.; Jang, J.; Kim, M. W.; Park, Y. Polarization Holographic Microscopy for Extracting Spatio-Temporally Resolved Jones Matrix. *Opt. Express* **2012**, *20* (9), 9948−9955.
(48) Jones, R. C. I. Description and Discussion of the Calculus. *J. Opt. Soc. Am.* **1941**, *31* (7), 488−493.
(49) Wang, Z.; Millet, L. J.; Gillette, M. U.; Popescu, G. Jones Phase Microscopy of Transparent and Anisotropic Samples. *Opt. Lett.* **2008**, *33* (11), 1270.
(50) Lee, T.; Senyuk, B.; Trivedi, R. P.; Smalyukh, I. I. Polarization Holographic Microscopy for Extracting Spatio-Temporally Resolved Jones Matrix. *Fluids, Colloids and Soft Materiels: An Introduction to Soft Matter Physics*; Wiley, 2018; Vol. *20*, Iss 9, pp 165−186,
(51) Zhou, S. Elasticity, Viscosity, and Orientational Fluctuations of a Lyotropic Chromonic Nematic Liquid Crystal Disodium Cromoglycate. *Lyotropic Chromonic Liquid Crystals*; Springer, 2017; pp 13−31, DOI: 10.1007/978-3-319-52806-9.

https://doi.org/10.1021/acsphotonics.1c00788
ACS Photonics 2021, 8, 3440−3447